

# Low-latitude mesopelagic nutrient recycling controls productivity and export

<https://doi.org/10.1038/s41586-024-07779-1>

Received: 10 September 2023

Accepted: 2 July 2024

Published online: 21 August 2024

 Check for updates

Keith B. Rodgers<sup>1</sup>✉, Olivier Aumont<sup>2</sup>✉, Katsuya Toyama<sup>3</sup>, Laure Resplandy<sup>4,5</sup>, Masao Ishii<sup>3</sup>, Toshiya Nakano<sup>6</sup>, Daisuke Sasano<sup>7</sup>, Daniele Bianchi<sup>8</sup> & Ryohei Yamaguchi<sup>9</sup>

Low-latitude (LL) oceans account for up to half of global net primary production and export<sup>1–5</sup>. It has been argued that the Southern Ocean dominates LL primary production and export<sup>6</sup>, with implications for the response of global primary production and export to climate change<sup>7</sup>. Here we applied observational analyses and sensitivity studies to an individual model to show, instead, that 72% of LL primary production and 55% of export is controlled by local mesopelagic macronutrient cycling. A total of 34% of the LL export is sustained by preformed macronutrients supplied from the Southern Ocean via a deeper overturning cell, with a shallow preformed northward supply, crossing 30° S through subpolar and thermocline water masses, sustaining only 7% of the LL export. Analyses of five Coupled Model Intercomparison Project Phase 6 (CMIP6) models, run under both high-emissions low-mitigation (shared socioeconomic pathway (SSP5-8.5)) and low-emissions high-mitigation (SSP1-2.6) climate scenarios for 1850–2300, revealed significant across-model disparities in their projections of not only the amplitude, but also the sign, of LL primary production. Under the stronger SSP5-8.5 forcing, with more substantial upper-ocean warming, the CMIP6 models that account for temperature-dependent remineralization promoted enhanced LL mesopelagic nutrient retention under warming, with this providing a first-order contribution to stabilizing or increasing, rather than decreasing, LL production under high emissions and low mitigation. This underscores the importance of a mechanistic understanding of mesopelagic remineralization and its sensitivity to ocean warming for predicting future ecosystem changes.

The low-latitude (LL) ocean regions, considered to be the expanse between the subtropical convergence zones (30° S–30° N), are important for their rich biodiversity, as well as for fisheries and food security<sup>8–10</sup>. Both LL marine primary productivity (PP) and export account for up to half of their global totals<sup>1–5</sup>. High PP and export occur despite thermocline concentrations being less than half of what is found in subpolar and circumpolar regions, reflecting the vigorous decadal renewal of LL thermocline waters<sup>11–13</sup>. A long-standing paradigm<sup>6</sup> maintains that preformed nutrients exported from the Southern Ocean below the thermocline, in subantarctic-mode water (SAMW), sustain 75% of LL new production through LL upwelling. A subsequent study, using an inverse ocean biogeochemical model<sup>14</sup>, identified 44% of export north of 40° S as being the consequence of Southern Ocean nutrient trapping, arguing for a first-order role for the Southern Ocean. However, independent observational analyses have indicated that, at least for the Pacific, SAMW cannot readily access regions north of 20° S due to strong potential vorticity barriers<sup>15</sup>.

A simulation using an Earth system model (ESM) under strong anthropogenic forcing (historical forcing followed by representative concentration pathway RCP8.5) has indicated that LL export and PP could decrease by 41% and 24%, respectively, by 2300<sup>7</sup>. This collapse, initially triggered by a southward shift in Southern Ocean westerlies and sea-ice retreat, has been argued to precipitate subsurface Southern Ocean nutrient trapping, thereby reducing nutrient export northward to the LLs via SAMW. This ESM study was important in emphasizing the LL responses in PP and export under multi-century climate perturbations. However, although it invoked the long-standing paradigm for the mechanisms<sup>6</sup>, it did not quantify the disruptions in LL nutrient supply. With the available Coupled Model Intercomparison Project Phase 6 (CMIP6) models—the low-resolution version of the Institut Pierre-Simon Laplace Climate Model (IPSL-CM6A)<sup>16</sup>, Community ESM Version 2–Whole Atmosphere Community Climate Model (CESM2-WACCM)<sup>17</sup>, United Kingdom Earth System Model version 1 (UKESM1)<sup>18</sup>, Australian Community Climate and Earth System Simulator–Earth System Model Version 1.5 (ACCESS-ESM1.5)<sup>19</sup> and

<sup>1</sup>WPI-Advanced Institute for Marine Ecosystem Change, Tohoku University, Sendai, Japan. <sup>2</sup>Sorbonne Universités, UPMC, Univ. Paris 06-CNRS-IRD-NHNN, LOCEAN/IPSL, Paris, France.

<sup>3</sup>Climate and Geochemistry Research Department, Meteorological Research Institute, Japan Meteorological Agency, Tsukuba, Japan. <sup>4</sup>Princeton University, Department of Geosciences, Princeton, NJ, USA. <sup>5</sup>Princeton University High Meadows Environmental Institute, Princeton, NJ, USA. <sup>6</sup>Nagasaki Ocean Academy, NPO Nagasaki Marine Industry Cluster Promotion Association, Nagasaki, Japan. <sup>7</sup>Atmosphere and Ocean Department, Japan Meteorological Agency, Tokyo, Japan. <sup>8</sup>Department of Atmospheric and Oceanic Sciences, University of California, Los Angeles, Los Angeles, CA, USA. <sup>9</sup>Research Institute for Global Change, Japan Agency for Marine-Earth Science and Technology, Yokosuka, Japan. ✉e-mail: keith.rodgers.b2@tohoku.ac.jp; olivier.aumont@ird.fr

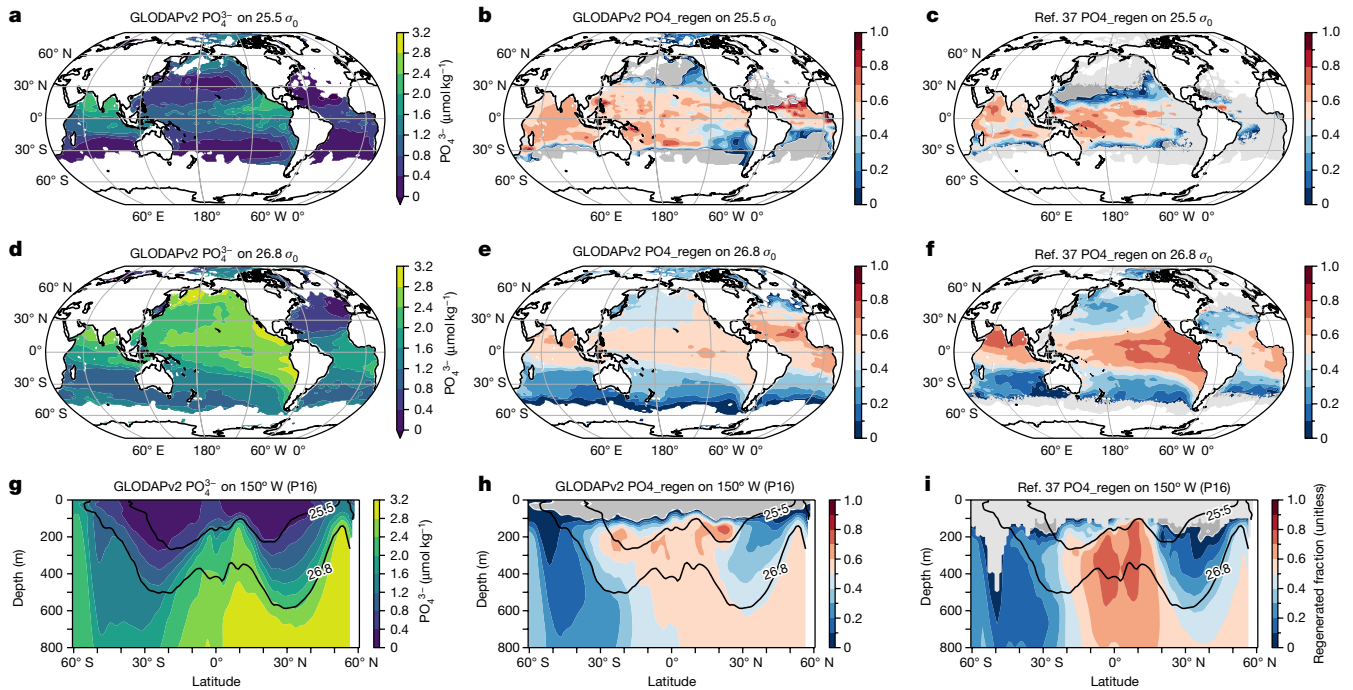


**Fig. 1 | Regenerated fraction of  $\text{PO}_4^{3-}$  from observation-anchored products.**

**a,d,g**, The  $\text{PO}_4^{3-}$  distributions from GLODAPv2 (refs. 23,24). **b,e,h**, The regenerated fraction of  $\text{PO}_4^{3-}$  [ $\text{PO}_4_{\text{regen}} = (\text{PO}_4^{3-} - \text{PO}_4^{3-*})/\text{PO}_4^{3-}$ ], calculated using GLODAPv2 with a stoichiometric ratio ( $-\text{O}_2:\text{PO}_4^{3-}$ ) of 170:1, with  $\text{PO}_4^{3-}$  representing the preformed concentration. **c,f,i**, The regenerated fraction of  $\text{PO}_4^{3-}$  calculated through the combined use of the GLODAPv2  $\text{PO}_4^{3-}$  and a separate preformed  $\text{PO}_4^{3-}$  product<sup>37</sup>. **a–c**, The property distributions at the mid-thermocline ( $\sigma_0 = 25.5 \text{ kg m}^{-3}$ ) horizon. **d–f**, The property distributions

on the upper boundary ( $\sigma_0 = 26.8 \text{ kg m}^{-3}$ ) of the SAMW layer. **g–i**, The property distributions along  $150^\circ\text{W}$  in the Pacific Basin. Dark grey shading in **h** indicates regions with negative  $\text{PO}_4_{\text{regen}}$ , with darker grey shading in **i** denoting regions where preformed  $\text{PO}_4^{3-}$  was not defined<sup>37</sup>. Near  $50^\circ\text{S}$ , the grey intrusion to 500 m marks where the seasonal boundary layer is deep. P16 designates a meridional cruise track where measurements were made along  $150^\circ\text{W}$  in the Pacific Ocean. The colour-bar label in **i** also applies to panels **b,c,e,f,h**.

Model for Interdisciplinary Research on Climate–Earth System Version 2 for Long-term simulations (MIROC-ES2L)<sup>20</sup>—run under historical forcing and both high-emissions low-mitigation (shared socioeconomic pathway (SSP) 5·8·5) and low-emissions high-mitigation (SSP1·2·6) scenarios<sup>21</sup> for 1850–2300, we were able to address the model-dependence of the earlier study. Under SSP5·8·5, the LL PP perturbations in the 2290s, relative to 1850–1899, were  $0.034 \pm 8.613 \text{ PgC yr}^{-1}$ , with pronounced uncertainty reflecting differences in both the amplitude and sign of the responses. Under SSP1·2·6, the LL PP perturbation in the 2290s was  $0.099 \pm 0.957 \text{ PgC yr}^{-1}$ , again with pronounced uncertainty. Remarkably, by the 2290s, the model structural uncertainty in PP for the LLs under either SSP5·8·5 ( $\pm 8.613 \text{ PgC yr}^{-1}$ ) or SSP1·2·6 ( $\pm 0.957 \text{ PgC yr}^{-1}$ ) was much larger than the scenario uncertainty ( $| -0.034 - 0.099 | = 0.133 \text{ PgC yr}^{-1}$ ), underscoring the importance of understanding the drivers of model structural uncertainty.

Here we used a combination of observations and models to argue, instead, for the importance of local LL processes in sustaining LL PP and export. More specifically, we propose that remineralization in the LL mesopelagic domain (LLMD) (defined as spanning  $30^\circ\text{S}$ – $30^\circ\text{N}$  and 150–870 m) and the rapid re-emergence of nutrients through shallow overturning structures, including the subtropical cells<sup>22</sup>, are the dominant processes. This framework rests on two related ideas—that warm LL thermocline waters are efficient in retaining nutrients and returning them to the euphotic zone, and that deeper upwelling across the base of the LLMD replenishes nutrients in the LL domain.

## Elevated tropical regenerated nutrients

We began by assessing the regenerated phosphate ( $\text{PO}_4^{3-}$ ) fraction in the LLs using two products derived from the Global Ocean Data Analysis Project Version 2 (GLODAPv2)<sup>23,24</sup> observational synthesis product.

The first assumes fixed stoichiometry, the second utilizes transport matrix output from an ocean circulation inverse model<sup>25</sup> without assuming fixed stoichiometry (Methods). The distributions of  $\text{PO}_4^{3-}$  at the mid-thermocline ( $\sigma_0 = 25.5 \text{ kg m}^{-3}$ ) (Fig. 1a) and on the upper boundary of the SAMW ( $\sigma_0 = 26.8 \text{ kg m}^{-3}$ ) (Fig. 1d) revealed concentrations that were at a maximum in the equatorial band, with both regenerated fraction estimates exceeding 50% over most of the LLs (Fig. 1b,c,e,f). Viewed along  $150^\circ\text{W}$  in the Pacific, despite large thermocline gradients in the  $\text{PO}_4^{3-}$  (Fig. 1g), the regenerated fraction exhibited remarkable homogeneity for both estimates (Fig. 1h,i), and exceeded 50% over  $10^\circ\text{S}$ – $10^\circ\text{N}$  and 150–700 m. If the fixed stoichiometric ratio proposed by Redfield<sup>26</sup> of a  $-\text{O}_2:\text{P}$  of 138:1 is used, the remineralized fraction becomes larger than that shown in the middle column of Fig. 1.

We hypothesized that this large regenerated LL nutrient pool exerts a dominant control on the elevated aggregated LL PP and export via local processes. To test this, we applied a set of perturbation simulations using the Pelagic Interactions Scheme for Carbon and Ecosystem Studies Volume 2 (PISCES-v2) biogeochemistry model<sup>27</sup> (Methods) that all employed identical circulation fields but that varied by perturbing the nutrient remineralization in distinct latitudinal bands. In addition to an unperturbed standard experiment (STD), we performed perturbation experiments in which remineralization was disallowed within the LLs (PERT\_TROP) over the depths involved in wind-driven circulation (150–1,500 m) and over the southern ( $90^\circ$ – $30^\circ\text{S}$ ) (PERT\_SOUTH) and northern ( $30^\circ$ – $90^\circ\text{N}$ ) (PERT\_NORTH) hemispheres. For PERT\_SOUTH and PERT\_NORTH, remineralization was disallowed in the interior, such that nutrients could only remineralize at depth in the bottom grid box.

A comparison of the STD and PERT\_TROP experiments revealed a large reduction in LL PP and export when local mesopelagic remineralization was disallowed (Fig. 2). For STD, the net LL PP and export were 22.7 and  $2.74 \text{ PgC yr}^{-1}$ , respectively. For PERT\_TROP,

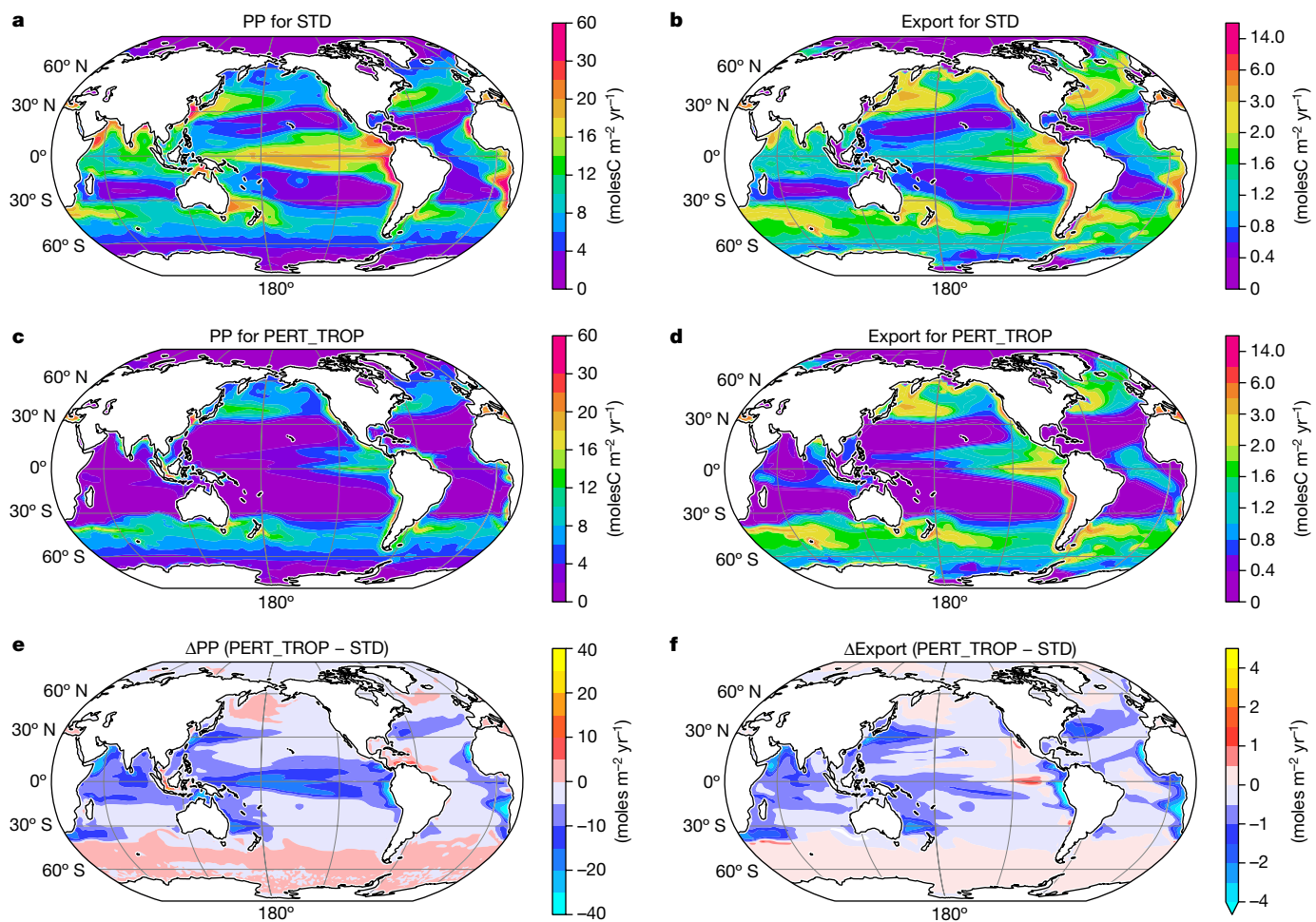


**Fig. 2 | Model-derived sensitivity of PP and export to the suppression of nutrient regeneration over the LLs.** The PISCES-v2 (ref. 27) model sensitivity for PP and export at 150 m to the suppression of nutrient regeneration over the LL region, spanning 30° S–30° N and 150–1,500 m. **a**, Annual mean PP for the STD experiment. **b**, Annual mean export for the STD experiment. **c**, PP for the

PERT\_TROP experiment. **d**, Export for the PERT\_TROP experiment. **e**, Difference in PP between PERT\_TROP and STD. **f**, Difference in export between PERT\_TROP and STD. PP was considered for full-depth integrals, with export considered at 150 m, this being the upper boundary defined for the LLMD shown in Fig. 3.

the net LL PP and export were 6.40 and 1.24 PgC  $\text{yr}^{-1}$ , respectively. Thus, PERT\_TROP represented a 72% drop in LL PP and a 55% drop in LL export relative to the STD. These changes are larger than the 30% reduction in PP and 40% decrease in export with PERT\_SOUTH (PERT\_SOUTH and PERT\_NORTH are shown in Extended Data Figs. 1 and 2, respectively, and the zonal mean  $\text{PO}_4^{3-}$  is shown in Extended Data Figs. 3 and 4).

The strong sensitivity of PERT\_TROP relative to STD was addressed by coarse-graining the modelled  $\text{PO}_4^{3-}$  budget in the LLMD (Fig. 3, with all four simulations shown in Extended Data Fig. 5). For STD (black) the soft-tissue flux across 870 m was 0.89 PgC  $\text{yr}^{-1}$  (the dissolved organic phosphorus fluxes were negligible), with a net remineralization source within the LLMD (the largest in the shallow thermocline) of 1.98 PgC  $\text{yr}^{-1}$ . For PERT\_TROP (red) with disallowed LL remineralization over 150–1,500 m, the interior production was  $-0.16 \text{ PgC yr}^{-1}$  due to PP occurring just below 150 m. The upward flux of  $\text{PO}_4^{3-}$  across 870 m increased by 0.09 PgC  $\text{yr}^{-1}$ , with a net reduction of meridional divergence across 30° S–30° N of 0.34 PgC  $\text{yr}^{-1}$ , indicating that under PERT\_TROP, the system damped the perturbation by increasing the supply from below—a feedback that boosted LLMD nutrient retention. The lateral meridional fluxes between 0 m and 150 m at 30° S and 30° N were nearly zero, as these boundaries correspond to the subtropical convergence zones, where meridional surface Ekman transports reach a minimum.

## Deep Southern Ocean nutrient supply path

For STD, the net (sum of northward and southward) meridional fluxes of  $\text{PO}_4^{3-}$  across 30° S and 30° N present a divergence that depletes  $\text{PO}_4^{3-}$  over the LLMD. When the LLMD accumulation is disrupted (PERT\_TROP), divergence decreases. The horizontal divergence identified by STD for the LLMD is opposite in sign to that implied in the long-standing paradigm<sup>6</sup>. Further simulations, with idealized representations of regenerated and preformed  $\text{PO}_4^{3-}$ , were conducted using PISCES-v2, following a method from an earlier study<sup>14</sup> (Methods), which enabled attribution (these results are summarized in Extended Data Table 1). The net upward transport of  $\text{PO}_4^{3-}$  across 150 m was dominated by a 65% regenerated component, of which 82% was generated in the LLs. Thus, 53% (representing the product) and a majority of LL export was due to LLMD nutrient regeneration. Of the 35% preformed  $\text{PO}_4^{3-}$  contribution to LL export, approximately 98% was Southern Ocean-sourced, largely (78%) through upwelling from deeper layers across 870 m. Consequently, only 7% of the LL export could be accounted for by the northward transport of preformed  $\text{PO}_4^{3-}$  across 30° S in the SAMW and thermocline layers, whereas the contribution to LL export of nutrients regenerated in the LLs, at 53%, was seven to eight times greater than the contribution from the mechanism highlighted in the long-standing paradigm<sup>6</sup>.

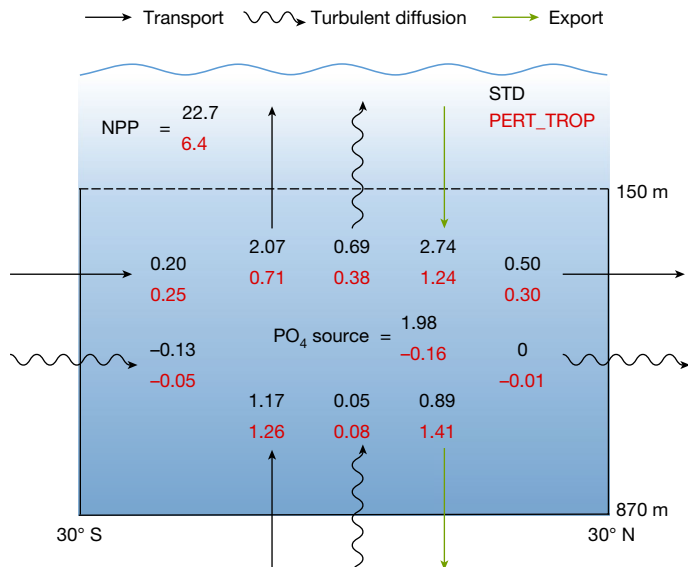


**Fig. 3 | Coarse-grained view of modelled PO<sub>4</sub><sup>3-</sup> fluxes about the LLMD.** For PISCES-v2 (ref. 27), the boundary fluxes and interior sources of PO<sub>4</sub><sup>3-</sup> are shown as a coarse-graining of the domain bounded by 30° S–30° N and 150–870 m, comparing STD (black) and PERT\_TROP (red) cases with the PISCES-v2 shown in Fig. 2. The lateral boundary fluxes for the domain represent net fluxes, thereby accounting for the effects of gyre recirculation across 30° S and 30° N. The net horizontal convergence of PO<sub>4</sub><sup>3-</sup> across the meridional boundaries at 30° S and 30° N is −0.43 PgC yr<sup>−1</sup> for STD and −0.09 PgC yr<sup>−1</sup> for PERT\_TROP, indicating a net flux out of the LLMD across these meridional boundaries. The transfer efficiency for STD—defined as the ratio of export flux across 870 m to the export flux across 150 m—is 32%. The fluxes are for PO<sub>4</sub><sup>3-</sup> but they are shown in carbon units of PgC yr<sup>−1</sup> to be consistent with the units typically used for export and the biological pump. The carbon:phosphorus ratio used here to convert PO<sub>4</sub><sup>3-</sup> into carbon units was 122:1 (Methods).

The PERT\_TROP perturbation relative to STD (Fig. 3) underscores that the dominant process sustaining elevated aggregated LL PP and export is the remineralization of PO<sub>4</sub><sup>3-</sup> in the local LLMD and its subsequent local re-emergence into the euphotic zone through shallow overturning. The remineralized LL pool is contingent on the background upward supply of nutrients across the base of the LLMD through the upwelling of deeper waters, not only for balancing the downward particle flux across 870 m, but also in compensating for the net meridional divergence of PO<sub>4</sub><sup>3-</sup> out of the LLMD across 30° S and 30° N. The net upwelling of 8 sverdrups (Sv) across 870 m in the LLs (Extended Data Fig. 6) in the modelled circulation draws from a Southern Ocean ventilation source for the Indo-Pacific LLMD and a North Atlantic source for the Atlantic LLMD. This behaviour is consistent with the deeper LL upwelling that has been identified with observational constraints<sup>28</sup> and other models<sup>29,30</sup>. In fact, the main impact of our PERT\_SOUTH experiment was to enhance the net divergence (0.14 Pg yr<sup>−1</sup> relative to STD) of the regenerated PO<sub>4</sub><sup>3-</sup> pool from the LLs (Extended Data Fig. 5).

The 40% drop in LL export simulated in PERT\_SOUTH is consistent with the sensitivity identified in an earlier study using a data-assimilating model<sup>14</sup>. However, that study did not consider or quantify LL remineralization as a primary driver. A separate study<sup>31</sup> that applied nutrient restoration<sup>6</sup> acknowledged that remineralized LL nutrients sustained new LL production, but only under the assumption that this pool represented a downstream legacy of preformed nutrients supplied by SAMW. That study ruled out both a first-order role for local LL regeneration processes and an LL upwelling source of deeper waters.

Having identified the critical role of LL remineralization using a single model (Fig. 3), we redirected our attention to the PP perturbations in the five CMIP6 ESMs<sup>16–20</sup> run to 2300 under historical forcing and then

high-emissions and low-mitigation (SSP5-8.5) and low-emissions and high-mitigation (SSP1-2.6) pathways<sup>21</sup>. Under SSP5-8.5, global (Fig. 4a) and LL (Fig. 4b) integrated PP perturbations, relative to 1850–1899, revealed that the ranking of PP anomalies by model at global scales was largely determined in the LLs, with the LL responses by the 2290s being  $-0.034 \pm 8.613 \text{ PgC yr}^{-1}$  for SSP5-8.5 and  $0.099 \pm 0.957 \text{ PgC yr}^{-1}$  for SSP1-2.6 (the temperature fields for SSP5-8.5 are shown in Extended Data Fig. 7). The model structural uncertainty under SSP5-8.5, of 8.613 PgC yr<sup>−1</sup>, was much greater than the scenario uncertainty (the difference between the model means for SSP1-2.6 and SSP5-8.5) of 0.13 PgC yr<sup>−1</sup>. It is conventionally assumed that individual model trajectories represent equally likely outcomes under the imposed climate forcing, with the response reflecting an underlying diversity of model parameterizations for unresolved processes<sup>32,33</sup>. Because the increase in PP over the LLs for two of the models (IPSL-CM6A and ACCESS-ESM1.5) was not, at face value, consistent with the long-standing paradigm<sup>6</sup>—with a disrupted SAMW supply of nutrients triggered by shifting Southern Ocean winds<sup>7</sup> (Extended Data Fig. 8)—we considered whether the nutrient-recycling mechanism highlighted in Figs. 2 and 3 may have contributed to the differences.

## Divergent nutrient retention in ESMs

To this end, we considered the fractional changes in zonal mean ocean interior PO<sub>4</sub><sup>3-</sup> concentrations under historical/SSP5-8.5 forcing for the IPSL-CM6A (Fig. 4c) (increasing LL PP) and CESM2-WACCM (Fig. 4d) (decreasing LL PP) models between the 1990s and 2290s. Using both models, the transfer efficiency mean for the 1990s (the ratio of the soft-tissue flux at 870 m relative to 150 m) was 26–27% for both IPSL-CM6A and CESM2-WACCM over the LLs (Extended Data Table 2). However, by the 2290s, the transfer efficiency over the LLs had reduced to 21% for IPSL-CM6A (enhanced thermocline nutrient retention) and had increased to 30% for CESM2-WACCM (decreased thermocline nutrient retention), as reflected in the fractional perturbations (2290s relative to 1990s) to the zonally averaged PO<sub>4</sub><sup>3-</sup> for both models, shown in Fig. 4c,d, respectively. The difference between the two models reflects the fact that the remineralization in IPSL-CM6A responded to transients in mesopelagic temperature, whereas in CESM2-WACCM it did not<sup>34</sup>. As such, these differences in the representations of remineralization and the ensuing thermocline nutrient retention contributed to a modest increase in export for IPSL-CM6A of 0.3% by the year 2300 and a reduction of 38% for CESM2-WACCM under sustained SSP5-8.5 forcing. These results are robust under the SSP1-2.6 climate mitigation scenario (Extended Data Table 2) for both IPSL-CM6A and CESM2-WACCM. Under the weaker forcing, both the LLMD transfer efficiency and nutrient retention were approximately 20% of that found under the stronger SSP5-8.5 scenario. This indicates that the LLMD's capacity to retain nutrients by the year 2300 was scaled with the amplitude of the large-scale climate perturbation.

## Conclusions

In light of our findings, the inter-model disagreement in long-term projections of PP to 2300 for CMIP6 models (Fig. 4b) has a first-order source in the representation of the temperature-dependence of remineralization, rather than representing a random accumulation of uncertainty across disparate model parameterizations. The importance of this temperature-dependence reflects the key role played by the large pool of PO<sub>4</sub><sup>3-</sup> remineralized in the LLMD, with this pool sustaining more than half of LL export, standing in stark contrast to the modest contribution of less than 10% from SAMW. This underscores the importance of an improved process-understanding of the temperature-dependence of remineralization in projecting future PP and export<sup>35</sup> and, as a consequence, the ability of marine ecosystems to sustain food provisions and other services<sup>36</sup>.

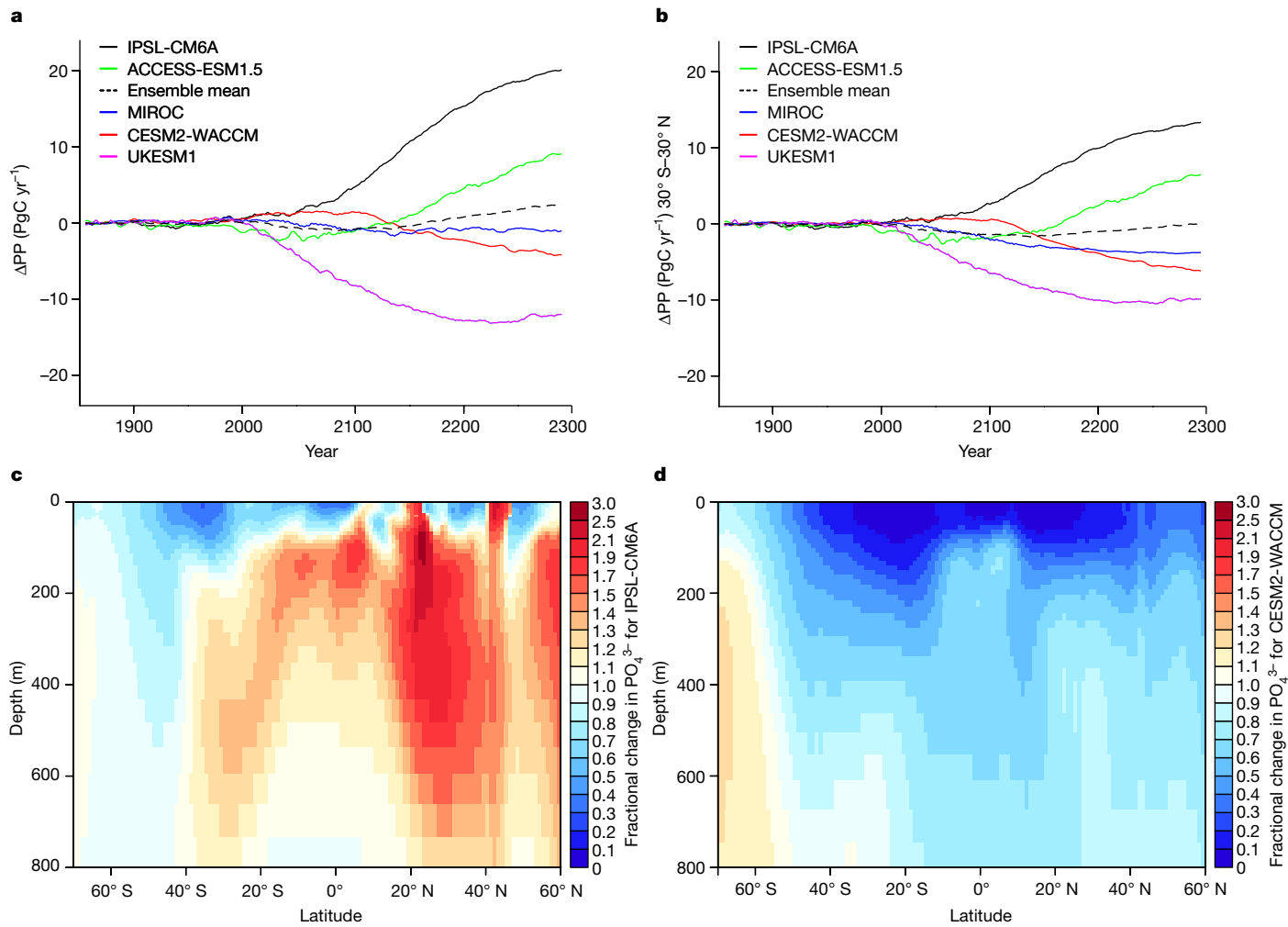


**Fig. 4 | Response of CMIP6 ESMs to sustained strong forcing to 2300.**

**a, b,** Evolution of changes (each relative to their respective 1850–1899 means) of globally integrated PP (**a**) and PP integrated over  $30^\circ\text{S}$ – $30^\circ\text{N}$  (**b**) for five CMIP6 models (IPSL-CM6A<sup>16</sup>, CESM2-WACCM<sup>17</sup>, UKESM1 (ref. 18), ACCESS-ESM1.5 (ref. 19) and MIROC-ES2L<sup>20</sup>), run to 2300 under historical and SSP5-8.5 forcing<sup>21</sup>. The model mean is shown as a dashed line, with the forced perturbations to

LL PP during the 2290s relative to 1850–1899 being  $-0.034 \pm 8.613 \text{ PgC yr}^{-1}$  for SSP5-8.5. **c, d,** Fractional changes in zonally averaged  $\text{PO}_4^{3-}$  concentrations between a 1990s and a 2290s climatology for two of the models—IPSL-CM6A (**c**) and CESM2-WACCM (**d**). The proportional  $\text{PO}_4^{3-}$  changes shown in **c** for IPSL-CM6A represent more than a doubling of the concentrations in the upper thermocline between the 1990s and 2290s.

## Online content

Any methods, additional references, Nature Portfolio reporting summaries, source data, extended data, supplementary information, acknowledgements, peer review information; details of author contributions and competing interests; and statements of data and code availability are available at <https://doi.org/10.1038/s41586-024-07779-1>.

1. Selsbe, G. M., Behrenfeld, M. J., Halsey, K. H., Milligan, A. J. & Westberry, T. K. The CAFE model: a net production model for global ocean phytoplankton. *Global Biogeochem. Cycles* **30**, 1756–1777 (2016).
2. Carr, M. E. et al. A comparison of global estimates of marine primary production from ocean color. *Deep-Sea Res. II: Top. Stud. Oceanogr.* **53**, 741–770 (2006).
3. Westberry, T. K., Behrenfeld, M. J., Siegel, D. A. & Boss, E. Carbon-based primary productivity modeling with vertically resolved photoacclimation. *Global Biogeochem. Cycles* **22**, e2007GB003078 (2008).
4. Nowicki, M., DeVries, T. & Siegel, D. A. Quantifying the carbon export and sequestration pathways of the ocean's biological carbon pump. *Global Biogeochem. Cycles* **36**, e2021GB007083 (2022).
5. Schlitzer, R. Applying the adjoint method for biogeochemical modeling: export of particulate organic matter in the world ocean. *Geophys. Monogr. Am. Geophys. Union* **114**, 107–124 (2000).
6. Sarmiento, J. L., Gruber, N., Brzezinski, M. A. & Dunne, J. P. High-latitude controls of thermocline nutrients and low latitude biological productivity. *Nature* **427**, 56–60 (2004).
7. Moore, J. K. et al. Sustained climate warming drives declining marine biological productivity. *Science* **359**, 1139–1142 (2018).
8. State of World Fisheries and Aquaculture: 2012 (FAO, 2012).
9. Costello, C. et al. The future of food from the sea. *Nature* **588**, 95–100 (2020).
10. Blanchard, J. L. et al. Linked sustainability challenges and trade-offs among fisheries, aquaculture and agriculture. *Nat. Ecol. Evol.* **1**, 1240–1249 (2017).
11. Fine, R. A., Mailett, K. A., Sullivan, K. F. & Willey, D. Circulation and ventilation flux of the Pacific Ocean. *J. Geophys. Res. Oceans* **106**, 22159–22178 (2001).
12. Aumont, O., Orr, J. C., Monfray, P., Madec, G. & Maier-Reimer, E. Nutrient trapping in the equatorial Pacific: the ocean circulation solution. *Global Biogeochem. Cycles* **13**, 351–369 (1999).
13. Toyama, K. et al. Large reemergence of anthropogenic carbon into the ocean's surface mixed layer sustained by the ocean's overturning circulation. *J. Clim.* **30**, 8615–8631 (2017).
14. Primeau, F. W., Holzer, M. & DeVries, T. Southern Ocean nutrient trapping and the efficiency of the biological pump. *J. Geophys. Res. Oceans* **118**, 2547–2564 (2013).
15. Hererra-Borreguero, L. & Rintoul, S. R. Subantarctic mode water: distribution and circulation. *Ocean Dyn.* **61**, 103–126 (2011).
16. Boucher, O. et al. Presentation and evaluation of the IPSL-CM6A-LR climate model. *J. Adv. Model. Earth Syst.* **12**, e2019MS002010 (2020).
17. Danabasoglu, G. et al. The community Earth system model version 2 (CESM2). *J. Adv. Model. Earth Syst.* **12**, e2019MS001916 (2020).
18. Sellar, A. A. et al. UKESM1: description and evaluation of the UK Earth system model. *J. Adv. Model. Earth Syst.* **11**, 4513–4558 (2019).
19. Ziehn, T. et al. The Australian earth system model: ACCESS-ESM1.5. *J. South. Hemisp. Earth Syst. Sci.* **70**, 193–214 (2020).
20. Hajima, T. et al. Development of the MIROC-ES2L Earth system model and the evaluation of biogeochemical processes and feedbacks. *Geosci. Model Dev.* **13**, 2197–2244 (2020).
21. Meinshausen, M. et al. The shared socio-economic pathway (SSP) greenhouse gas concentrations and their extensions to 2500. *Geosci. Model Dev.* **13**, 3571–3605 (2020).

22. McCreary, J. P. & Lu, P. Interaction between the subtropical and equatorial ocean circulations: the subtropical cell. *J. Phys. Oceanogr.* **24**, 466–497 (1994).
23. Olsen, A. et al. The Global Ocean Data Analysis Project version 2 (GLODAPv2) – an internally consistent data product for the world ocean. *Earth Syst. Sci. Data* **8**, 297–323 (2016).
24. Lauvset, S. K. et al. A new global interior ocean mapped climatology: the 1° x 1° GLODAP version 2. *Earth Syst. Sci. Data* **8**, 325–340 (2016).
25. DeVries, T. The oceanic anthropogenic CO<sub>2</sub> sink: storage, air-sea fluxes, and transports over the industrial era. *Global Biogeochem. Cycles* **28**, 631–647 (2014).
26. Redfield, A. C. The influence of organisms on the composition of seawater. *The Sea* **2**, 26–77 (1963).
27. Aumont, O., Ethe, C., Tagliabue, A., Bopp, L. & Gehlen, M. PISCES-v2: an ocean biogeochemical model for carbon and ecosystem studies. *Geosci. Model Dev.* **8**, 2465–2513 (2015).
28. Talley, L. D. Shallow, intermediate, and deep overturning components of the global heat budget. *J. Phys. Oceanogr.* **33**, 530–560 (2003).
29. Sen Gupta, A. et al. Future changes to the Indonesian throughflow and Pacific circulation: the differing role of wind and deep circulation changes. *Geophys. Res. Lett.* **43**, 1669–1678 (2016).
30. Feng, M., Zhang, X. B., Sloyan, B. & Chamberlain, M. Contribution of the deep ocean to the centennial changes of the Indonesian throughflow. *Geophys. Res. Lett.* **44**, 2859–2867 (2017).
31. Palter, J. B., Sarmiento, J. L., Gnanadesikan, A., Simeon, J. & Slater, R. D. Fueling export production: nutrient return pathways from the deep ocean and their dependence on the meridional overturning circulation. *Biogeosciences* **7**, 3549–3568 (2010).
32. Séférian, R. et al. Tracking improvement in simulated marine biogeochemistry between CMIP5 and CMIP6. *Curr. Clim. Change Rep.* **6**, 95–119 (2020).
33. Bopp, L. et al. Diazotrophy as a key driver of the response of marine net primary productivity to climate change. *Biogeosciences* **19**, 4267–4285 (2022).
34. Long, M. C. et al. Simulations with the Marine Biogeochemistry Library (MARBL). *J. Adv. Model. Earth Syst.* **13**, e2021MS002647 (2021).
35. Cram, J. A. et al. The role of particle size, ballast, temperature, and oxygen in the sinking flux to the deep sea. *Global Biogeochem. Cycles* **32**, 858–876 (2018).
36. Cooley, S. et al. in *Climate Change 2022: Impacts, Adaptation and Vulnerability* (eds Pörtner, H.-O. et al.) Ch. 3 (Cambridge Univ. Press, 2022).
37. Carter, B. R. et al. Preformed properties for marine organic matter and carbonate mineral cycling quantification. *Global Biogeochem. Cycles* **35**, e2020GB006623 (2021).

**Publisher's note** Springer Nature remains neutral with regard to jurisdictional claims in published maps and institutional affiliations.

Springer Nature or its licensor (e.g. a society or other partner) holds exclusive rights to this article under a publishing agreement with the author(s) or other rightsholder(s); author self-archiving of the accepted manuscript version of this article is solely governed by the terms of such publishing agreement and applicable law.

© The Author(s), under exclusive licence to Springer Nature Limited 2024

# Article

## Methods

### Observation-derived products

The analysis presented in Fig. 1 considered the resolubilized or regenerated fraction of  $\text{PO}_4^{3-}$  in the upper ocean. This property in the ocean interior reflects the net effect of  $\text{PO}_4^{3-}$  accumulation between its subduction and its arrival at a given ocean interior location in a water parcel, or more generally for a distribution of contributions in a parcel's ventilation history. This was considered for  $\text{PO}_4^{3-}$  rather than  $\text{NO}_3^-$  as the ocean interior's sources and sinks for  $\text{PO}_4^{3-}$  are simpler to evaluate and interpret. Importantly, the regenerated concentration of  $\text{PO}_4^{3-}$  is not directly measurable, but is rather inferred by first calculating a preformed  $\text{PO}_4^{3-}$  concentration and then differencing that from the full local  $\text{PO}_4^{3-}$  concentration.

To identify the resolubilized fractions of the nutrients in Fig. 1, we use two products— $\text{PO}_4^{3-}$  and other variables from GLODAPv2 (refs. 23,24) and a combination of the GLODAPv2 product for  $\text{PO}_4^{3-}$  and a different preformed  $\text{PO}_4^{3-}$  product<sup>37</sup>. The repeat hydrographic observational component of the global GLODAPv2 data product has been consistently quality-controlled for comparisons between cruises conducted by different laboratories and researchers.

All panels for  $\text{PO}_4^{3-}$  concentrations shown in Fig. 1a,d,g were taken directly from the GLODAPv2 product, including the temperature and salinity fields used to calculate the surface interior density, thereby facilitating views of properties on density horizons. Figure 1b,e,h were derived from the GLODAPv2 variables. There, a large pool of regenerated  $\text{PO}_4^{3-}$  was identified for the LLMD. The identification of this regenerated pool made use of a deconvolution of preformed and regenerated fractions of  $\text{PO}_4^{3-}$  using a long-standing method<sup>38,39</sup> employing the apparent oxygen utilization. We defined the regenerated fraction of  $\text{PO}_4^{3-}$  to be:

$$\text{PO}_4\text{-regen} = (\text{PO}_4^{3-} - \text{PO}_4^{3-*})/\text{PO}_4^{3-}$$

where  $\text{PO}_4^{3-*}$  is the preformed  $\text{PO}_4^{3-}$  concentration, inferred as:

$$\text{PO}_4^{3-*} = \text{PO}_4^{3-} - \text{AOU}/170.$$

The 170 denominator in the latter expression represents a widely used stoichiometric ratio<sup>40</sup>, and AOU denotes the apparent oxygen utilization. For smaller values of this denominator, such as the value of 138 from ref. 26, the preformed fraction becomes smaller, and thus the regenerated fraction becomes larger. When applying this framework to interior ocean fields, three assumptions are usually made: (1) the oxygen concentrations are at saturation with the atmospheric oxygen in the mixed layer of the ocean at the time of subduction; (2) the interior ocean circulation is predominantly a largely adiabatic process along constant density (isopycnal) horizons; and (3) there is a relatively constrained relationship between the rate of oxygen consumption and  $\text{PO}_4^{3-}$  production through respiration, such that a deconvolution of the preformed and regenerated fractions can be identified using temperature, salinity and oxygen concentrations, along with  $\text{PO}_4^{3-}$  concentrations.

Figure 1c,f,i were derived through the combined use of the GLODAPv2 product<sup>23,24</sup> for  $\text{PO}_4^{3-}$  and the second preformed  $\text{PO}_4^{3-}$  product<sup>37</sup>. The second product<sup>37</sup> calculates the preformed  $\text{PO}_4^{3-}$  by making combined use of the GLODAPv2 distribution and transport matrix output from a data-assimilating ocean circulation inverse model<sup>25</sup>. For the second product<sup>37</sup>, there is no imposition of stoichiometric ratios, these rather being part of the solution set of the method. They do not present preformed  $\text{PO}_4^{3-}$  in the upper 100 m of the ocean domain, but rather it is masked there. Thus, the distribution presented in Fig. 1c,f,i is undefined in regions where the depth of the  $\sigma_0 = 25.5 \text{ kg m}^{-3}$  density surface is less than 100 m.

### PISCES-v2 model simulations

The biogeochemical model applied to the mechanistic attribution and understanding was PISCES-v2 (ref. 27). The model was designed to simulate the lower trophic levels of ocean ecosystems (the phytoplankton, microzooplankton and mesozooplankton), as well as the marine biogeochemical cycling of carbon and the major nutrients (phosphorus, nitrogen, iron and silicon). The runs considered here represented the coupling of PISCES-v2 to a specific tripolar grid (denoted ORCA2) configuration of the Nucleus for European Modelling of the Ocean coupled to the Louvain-la-Neuve sea-ice model (NEMO-LIM) v.6. The ORCA2 configuration has a nominally 2° horizontal resolution, with a meridional refinement of 0.5° near the Equator, for 30 vertical levels. In PISCES-v2, the gravitational component of total organic carbon export from the euphotic zone to the interior of the ocean is represented by the gravitational sedimentation of two particulate pools that differ in their mean sizes, these pools distinguished by their sinking speeds. These particulate pools are continuously solubilized, dissolving organic matter based on a temperature-dependent rate. This dissolved pool is then ultimately remineralized into inorganic nutrients. As in the original publication of PISCES-v2, the PISCES-v2 simulations used here employed identical 5-day-averaged climatological physical-state variables to drive the biogeochemical model offline. Each of the four offline runs using PISCES-v2 described were run for more than 5,000 years. In the PISCES-v2 model, the stoichiometric ratio of C:N:P is 122:16:1 (ref. 41). Additionally, the  $-\text{O}_2:\text{P}$  ratio was from a separate study<sup>42</sup>, motivating the application of a ratio of  $-\text{O}_2:\text{P}$  of 166:1 in PISCES-v2.

In addition to the control (STD) simulation in PISCES-v2, three perturbation simulations were conducted by disallowing the solubilization of organic carbon,  $\text{PO}_4^{3-}$  and  $\text{NO}_3^-$  in the ocean interior in three specific latitudinal bands. We also deactivated flux feeding on particles by the mesozooplankton. The three perturbation simulations were denoted PERT\_NORTH, PERT\_SOUTH and PERT\_TROP. For PERT\_NORTH, this perturbation was applied over 30°–90° N, for PERT\_SOUTH, over 90°S–30° S, and for PERT\_TROP, over 30°S–30° N. For PERT\_NORTH and PERT\_SOUTH, remineralization and flux feeding were deactivated between the surface and bottom grid cells of the model to achieve the minimum possible  $\text{PO}_4^{3-}$  concentrations at the sea surface. The decision to use 150–1,500 m for the applied perturbation in PERT\_TROP was motivated by a need to avoid remineralization throughout the wind-driven circulation structures that include intermediate waters that extend to depths as great as 1,500 m, which contain a large pool of regenerated  $\text{PO}_4^{3-}$ . Because all other elements of the PISCES-v2 code were unchanged in all three perturbation simulations, some remineralization would still occur below 150 m—for instance, where the euphotic zone depth exceeded 150 m. The remineralization would largely be associated with the activity of zooplankton suspension feeding on organic matter, whether living (phytoplankton, zooplankton) or particles, with the remineralization occurring through zooplankton excretion. The more biological activity there is below 150 m, the greater this remineralization becomes. This remineralization source through excretion would be pertinent in PERT\_TROP, where the euphotic zone exceeds 150 m throughout most of the LL ocean, because a sharp drop in nutrient availability due to the imposed perturbation would lead to a highly oligotrophic LL ocean. This would, in turn, lead to a PP distribution that was deeper for PERT\_TROP than for the STD, which also held for the other model simulations. With these concerns in mind, we opted to activate grazing on organic particles in the mesopelagic domain for PERT\_TROP, so as to more cleanly disallow the regeneration of  $\text{PO}_4^{3-}$  in the LLMD.

In addition to the standard tracer suite for PISCES-v2, we introduced four additional diagnostic tracers into the model for the purposes of this study. The first two tracked the total global preformed  $\text{PO}_4^{3-}$  and the preformed  $\text{PO}_4^{3-}$  originating from the Southern Ocean, defined as the region south of 30° S. Using a previously applied method<sup>14</sup>, we restored

these tracers to the full simulated concentrations of  $\text{PO}_4^{3-}$  in the mixed layer using a strong restoring constant of 4 days. Subsequently, these tracers were transported passively in the ocean interior. The relative contribution of the Southern Ocean to the total preformed  $\text{PO}_4^{3-}$  transported into the LLs was thereby facilitated. Two additional tracers were applied to represent the regenerated component of  $\text{PO}_4^{3-}$  in the LL domain ( $30^\circ\text{S}$ – $30^\circ\text{N}$ ), these being a global regenerated  $\text{PO}_4^{3-}$  tracer and a regenerated tracer over the LL domain spanning  $30^\circ\text{S}$ – $30^\circ\text{N}$ . The concentrations of these two tracers were restored to zero in the mixed layer, whereas, in the interior, they were produced at the same rate of  $\text{PO}_4^{3-}$  regeneration from the remineralization of organic matter. We summarized the transport fluxes for the LLMD domain using these tracers in Extended Data Table 1, assuming zero meridional Ekman transport over the upper 150 m. This was justified by the fact that our domain was bounded by the subtropical convergence regions in either hemisphere ( $30^\circ\text{S}$  and  $30^\circ\text{N}$ ).

The meridional overturning stream functions for the Indo-Pacific (Extended Data Fig. 6a) and Atlantic (Extended Data Fig. 6b) provided important circulation context for the interpretation of our simulations. For the Indo-Pacific domain (Extended Data Fig. 6a), there was clearly a superposition of strong overturning in the thermocline subtropical cells<sup>22</sup>, with net equatorward inter-gyre exchange across  $15^\circ$  of latitude exceeding 40 Sv. There was also an approximate 6 Sv of upwelling across 870 m, and thus across the base of the LLMD, with the ventilation source for this water lying in the Southern Ocean. In the Atlantic Basin (Extended Data Fig. 6b), the Atlantic meridional overturning over the upper 2,000 m was associated with an LLMD upwelling of approximately 2 Sv across the LLMD base, with the ventilation source for this water lying in the high latitudes of the North Atlantic.

## Earth system models

Here we considered five ESMs from CMIP6 that spanned the full period 1850–2300 that included the ocean biogeochemistry fields needed to assess future changes in PP. We considered the output from CMIP6 contributions that included appropriate variables for both a strong warming scenario (historical/SSP5-8.5) and a mitigation scenario (historical/SSP1-2.6)<sup>21</sup>, with the future projections using concentration pathways for forcing.

The five models included IPSL-CM6A<sup>16</sup>, CESM2-WACCM<sup>17</sup>, UKESM1 (ref. 18), ACCESS-ESM1.5 (ref. 19) and MIROC-ES2L<sup>20</sup>. The initialization and spin-up procedures for each model are given in the respective ESM presentation papers. The modelled PP (variable ‘intpp’), ocean interior phosphate concentrations (variable ‘po4’), surface air temperature (variable ‘tas’) and sea-surface temperature (variable ‘tos’) were considered for each of these five ESMs in this study. For IPSL-CM6A and CESM2-WACCM, the three-dimensional export flux for carbon (variable ‘expc’) was available, and was used in Extended Data Table 2 to characterize and quantify nutrient retention by the thermocline.

The two ESMs that showed increasing PP over  $30^\circ\text{S}$ – $30^\circ\text{N}$  (Fig. 4b) under SSP5-8.5–IPSL-CM6A and ACCESS-ESM1.5—represented enhanced remineralization rates under sustained warming due to their remineralization parameterizations. The MIROC-ES2L model also exhibited enhanced remineralization under sustained LL warming, although the degree of warming in MIROC-ES2L was less than in the other models, reflecting a weaker climate sensitivity. However, of the two models in which LL PP decreased, CESM2-WACCM did not account for the impact of warming on remineralization, and UKESM1 represented only a weak effect of temperature changes on remineralization. The UKESM1 model represented two sinking particle classes (small and large), and temperature-dependence for remineralization only applied to small particles, with this largely limited to the upper 200 m of the water column.

For both the means and standard deviations of the LL PP perturbations for the 2290s described in the main text and shown in Fig. 4b,

we list here the perturbation budgets for each of the five ESMs for the 2290s (average over 2290–2299), relative to 1850–1899. Under SSP5-8.5 forcing, the LL PP perturbations were 6.404 PgC yr<sup>-1</sup> for ACCESS-ESM1-5, 13.360 PgC yr<sup>-1</sup> for IPSL-CM6A, -3.798 PgC yr<sup>-1</sup> for MIROC-ES2L, -9.908 PgC yr<sup>-1</sup> for UKESM1 and -6.230 PgC yr<sup>-1</sup> for CESM2-WACCM. In the case of SSP1-2.6 forcing, by the 2290s, the LL PP perturbations were -0.234 PgC yr<sup>-1</sup> for ACCESS-ESM1-5, 1.571 PgC yr<sup>-1</sup> for IPSL-CM6A, -0.305 PgC yr<sup>-1</sup> for MIROC-ES2L, -1.397 PgC yr<sup>-1</sup> for UKESM1 and 0.252 PgC yr<sup>-1</sup> for CESM2-WACCM.

For the global PP perturbations in the 2290s, relative to 1850–1899 (Fig. 4a), under SSP5-8.5 forcing, the values were 9.067 PgC yr<sup>-1</sup> for ACCESS-ESM1-5, 20.210 PgC yr<sup>-1</sup> for IPSL-CM6A, -1.023 PgC yr<sup>-1</sup> for MIROC-ES2L, -12.070 PgC yr<sup>-1</sup> for UKESM1 and -4.249 PgC yr<sup>-1</sup> for CESM2-WACCM. Under SSP1-2.6 forcing, the global PP perturbations were 0.283 PgC yr<sup>-1</sup> for ACCESS-ESM1-5, 2.515 PgC yr<sup>-1</sup> for IPSL-CM6A, 0.780 PgC yr<sup>-1</sup> for MIROC-ES2L, -1.368 PgC yr<sup>-1</sup> for UKESM1 and 0.588 PgC yr<sup>-1</sup> for CESM2-WACCM.

## Inclusion and ethics

The authors are fully committed to removing barriers to the inclusion of diversity in the conduct of scientific research.

## Data availability

The data that support the findings of this study are available from the corresponding authors upon reasonable request.

## Code availability

The code for the PISCES-v2 model is available at Zenodo (<https://zenodo.org/records/10554639>; <https://doi.org/10.5281/zenodo.10554639>)<sup>43</sup>. The model output and analysis code used in the study is available at Zenodo (<https://zenodo.org/records/11617863>; <https://doi.org/10.5281/zenodo.11617863>)<sup>44</sup>. The code used to analyse the data and generate figures was based on Ferret and Python. We used an open-license Python package (Cartopy, <https://scitools.org.uk/cartopy/docs/latest/index.html>) to draw the base maps for Figs. 1 and 2 and Extended Data Figs. 1 and 2. As stated on their website (<https://scitools.org.uk/cartopy/docs/latest/citation.html#data-copyright-table>, <https://www.naturalearth-data.com/about/terms-of-use/>), the map data are in the public domain and can be used in any manner, including modification of the content and design, electronic dissemination and offset printing.

38. Broecker, W. S. “NO”, a conservative water-mass tracer. *Earth Planet. Sci. Lett.* **23**, 100–107 (1974).
39. Ito, T. & Follows, M. J. Preformed phosphate, soft tissue pump and atmospheric CO<sub>2</sub>. *J. Mar. Res.* **63**, 813–839 (2005).
40. Anderson, L. A. & Sarmiento, J. L. Redfield ratios of remineralization determined by nutrient data analysis. *Global Biogeochem. Cycles* **8**, 65–80 (1994).
41. Takahashi, T., Broecker, W. S. & Langer, S. Redfield ratio based on chemical data from isopycnal surfaces. *J. Geophys. Res. Oceans* **90**, 6907–6924 (1985).
42. Paulmier, A., Kriest, I. & Oschlies, A. Stoichiometries of remineralisation and denitrification in global biogeochemical ocean models. *Biogeosciences* **6**, 923–935 (2009).
43. Aumont, O. & Rodgers, K. Low-latitude mesopelagic nutrient recycling controls on productivity and export. Zenodo <https://doi.org/10.5281/zenodo.10554639> (2024).
44. Rodgers, K. & Aumont, O. Analysis files for “Low-latitude mesopelagic nutrient recycling controls productivity and export”. Zenodo <https://doi.org/10.5281/zenodo.11617863> (2024).

**Acknowledgements** We would like to thank J. Sarmiento for his iterative feedback and constructive comments throughout the development of this project. We would also like to thank L. Kwiatkowski for his feedback and constructive comments. K.B.R. was supported by the World Premier International Research Center Initiative, MEXT, Japan. D.B. acknowledges support from US NSF grant OCE-1847687. K.T. and M.I. received support from the Japan Meteorological Research Institute research fund C4 for the study of ocean biogeochemistry and acidification. K.T. was also supported by a grant-in-aid for Transformative Research Areas, under grant no. JP24H02224 from the Ministry of Education, Culture, Sports, Science, and Technology, Japan. L.R. acknowledges funding support from a US NSF career award 2042672 and a Grand Challenge research award funded by the Princeton University High Meadows Environmental Institute. R.Y. was supported by JSPS KAKENHI grant number JP24H02221.

# Article

**Author contributions** Conceptualization: K.B.R., O.A. Methodology: K.B.R., O.A. Investigation: K.B.R., O.A., K.T., D.S. Visualization: K.B.R., O.A., K.T., R.Y. Writing—original draft: K.B.R., O.A. Writing—review and editing: K.B.R., O.A., K.T., L.R., M.I., T.N., D.S., R.Y., D.B.

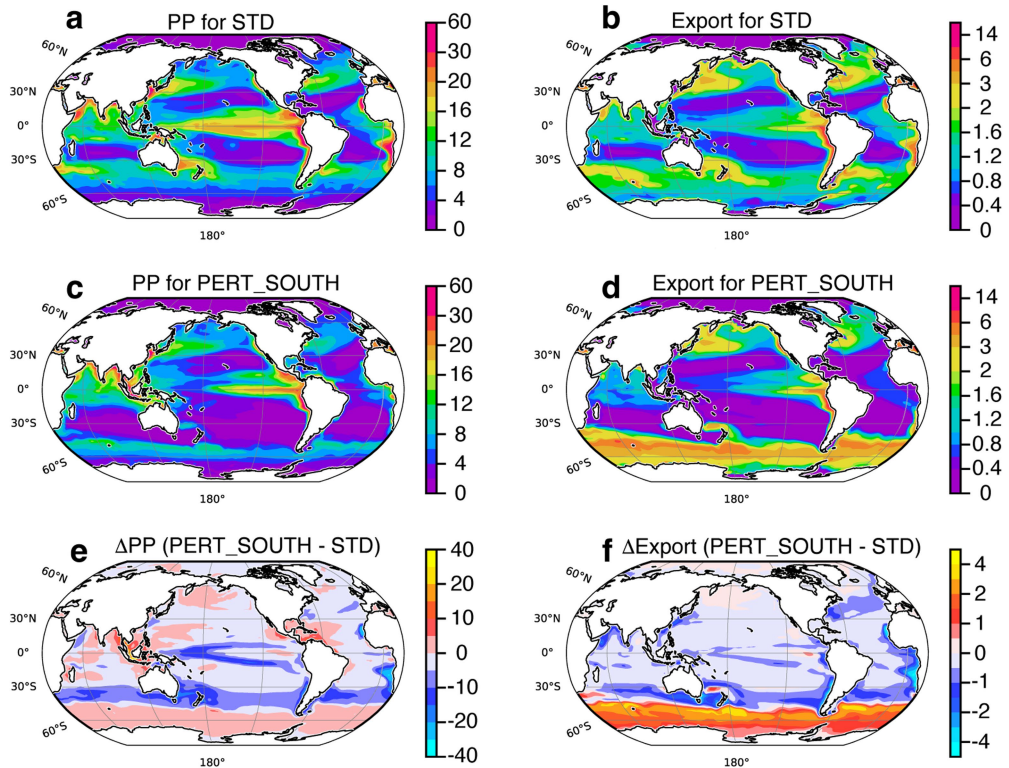
**Competing interests** The authors declare no competing interests.

## Additional information

**Correspondence and requests for materials** should be addressed to Keith B. Rodgers or Olivier Aumont.

**Peer review information** *Nature* thanks Robert Letscher and the other, anonymous, reviewer(s) for their contribution to the peer review of this work.

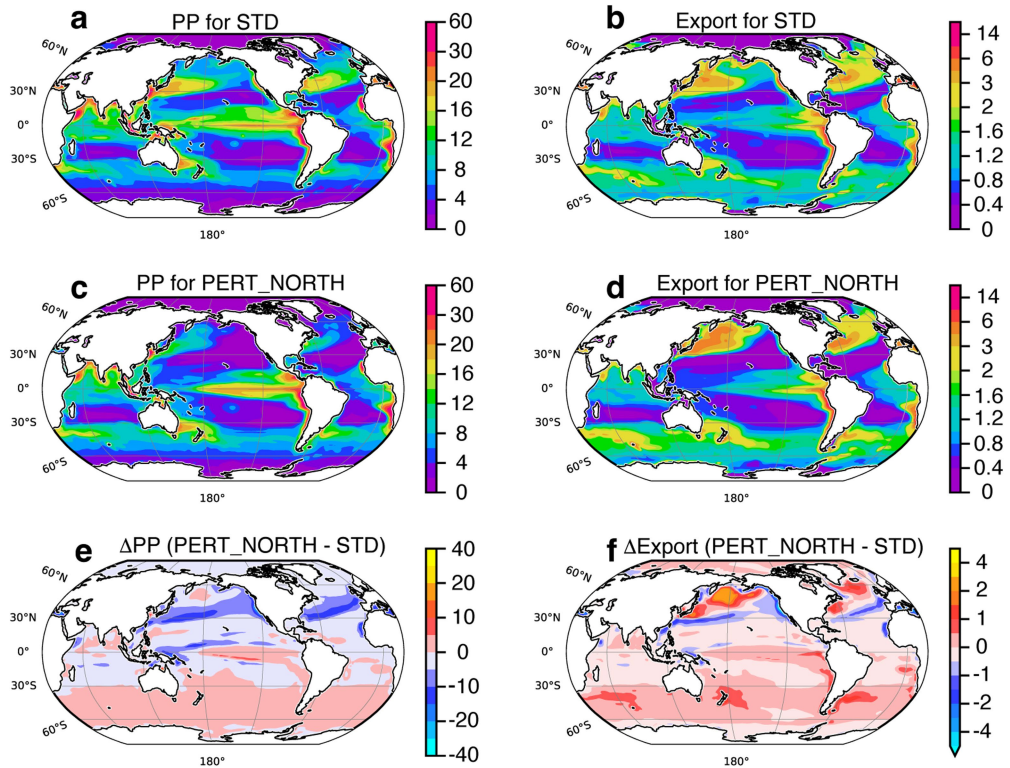
**Reprints and permissions information** is available at <http://www.nature.com/reprints>.



**Extended Data Fig. 1 | Model-derived sensitivity of primary production (PP) and export to suppression of nutrient regeneration over the Southern Ocean (PERT\_SOUTH) (90°S–30°S).** PISCES-v2<sup>27</sup> sensitivity for primary production (PP) and export to suppression of nutrient regeneration over the Southern Hemisphere extratropical domain 30°S–90°S. **(a)** Annual mean PP

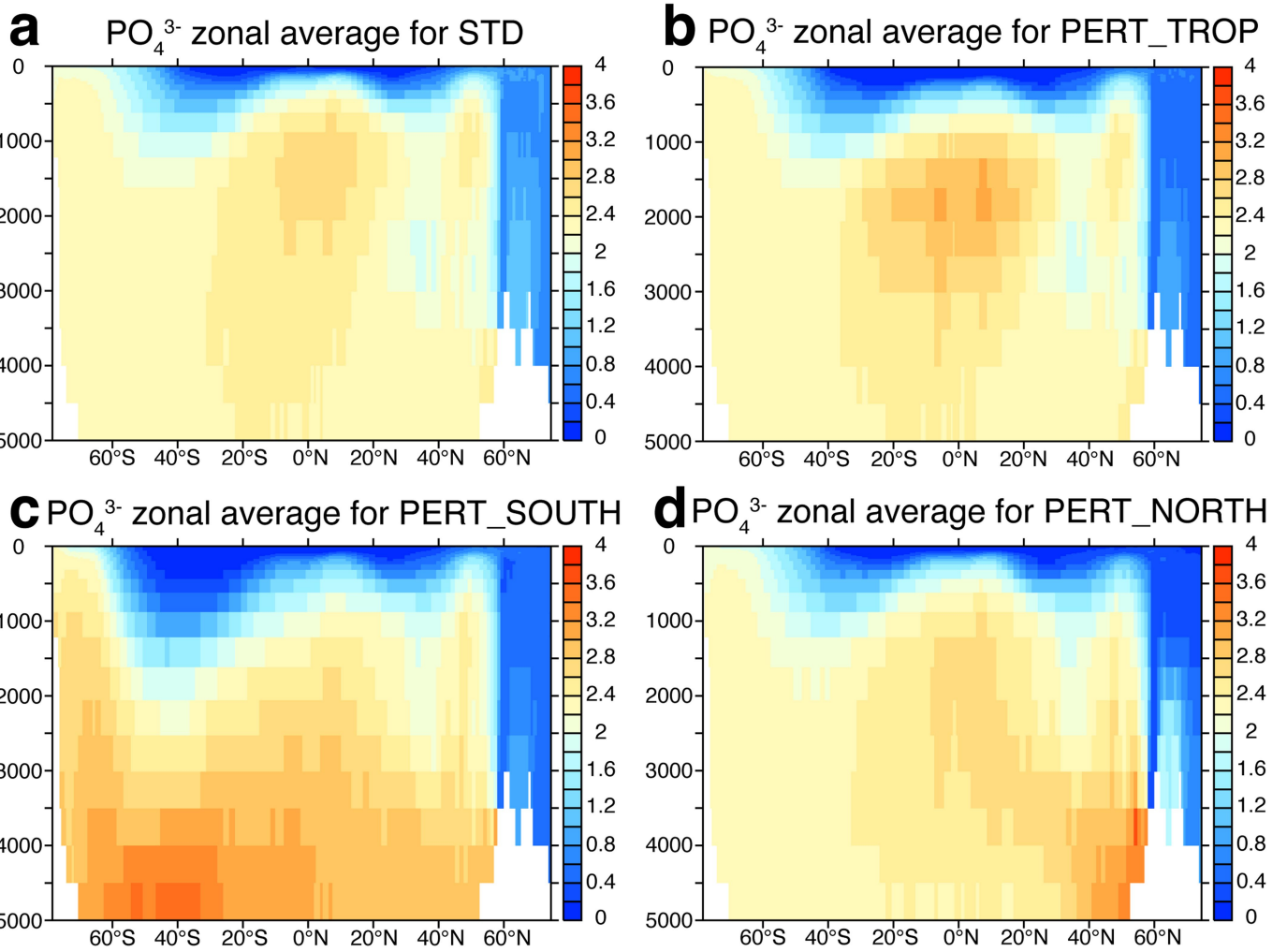
for control (STD) experiment; **(b)** annual mean export for STD experiment; **(c)** PP for PERT\_SOUTH experiment; **(d)** Export for PERT\_SOUTH experiment; **(e)** difference in PP between PERT\_SOUTH and STD; **(f)** difference in export between PERT\_SOUTH and STD. PP is considered for full-depth integrals, and export is considered at 150 m. Units are in moles C m<sup>-2</sup> yr<sup>-1</sup>.

# Article



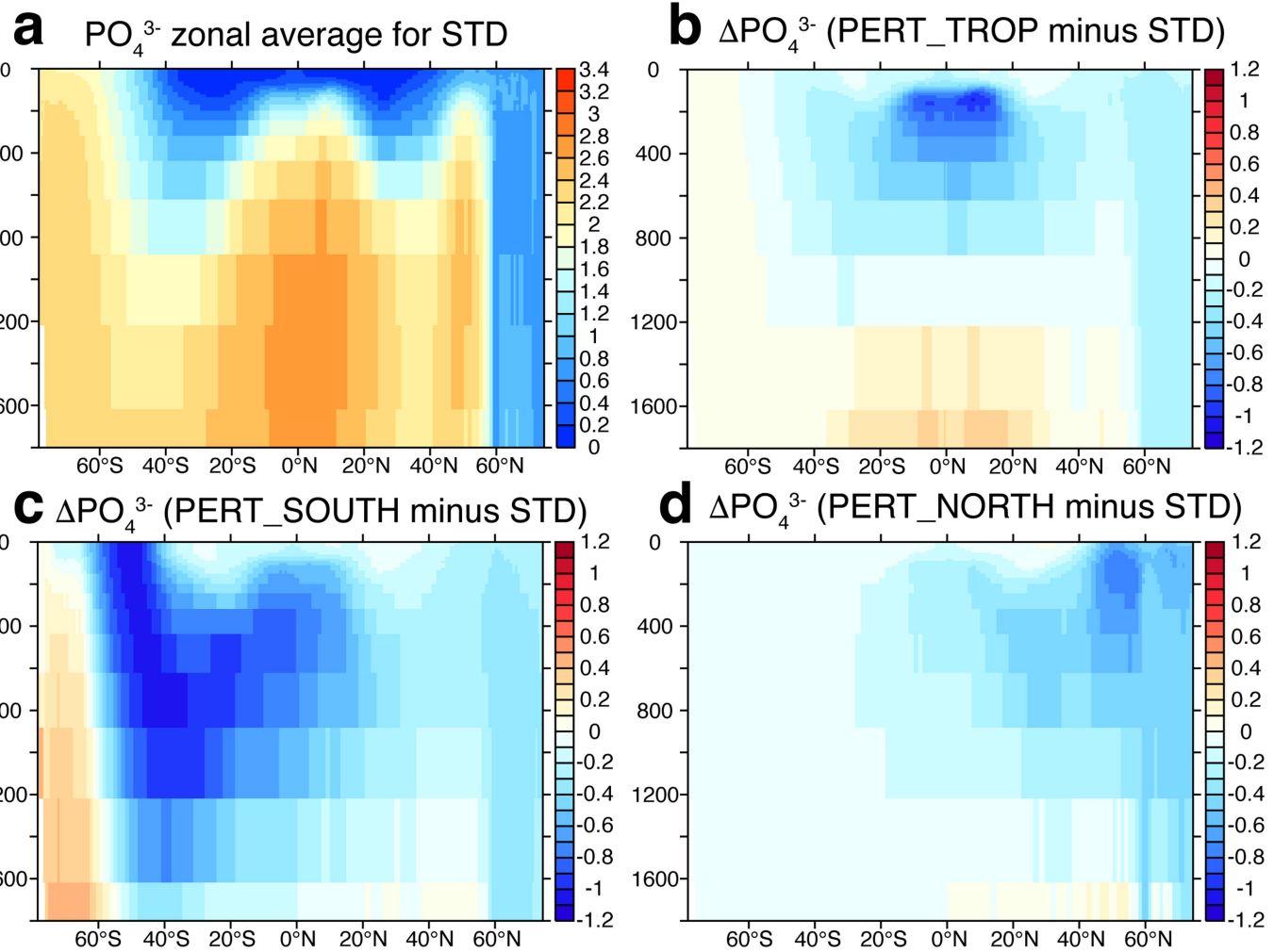
**Extended Data Fig. 2 | Model-derived sensitivity of primary production (PP) and export to suppression of nutrient regeneration over the northern oceans (PERT\_NORTH) (30°N–90°N).** PISCES-v2<sup>27</sup> sensitivity for primary production (PP) and export to suppression of nutrient regeneration over the Northern Hemisphere extratropical domain 30°N–90°N. (a) Annual mean PP

for control (STD) experiment, (b) annual mean export for STD experiment; (c) PP for PERT\_NORTH experiment; (d) Export for PERT\_NORTH experiment; (e) difference in PP between PERT\_NORTH and STD; (f) difference in export between PERT\_NORTH and STD. PP is considered for full-depth integrals, and export is considered at 150 m. Units are in moles C m<sup>-2</sup> yr<sup>-1</sup>.



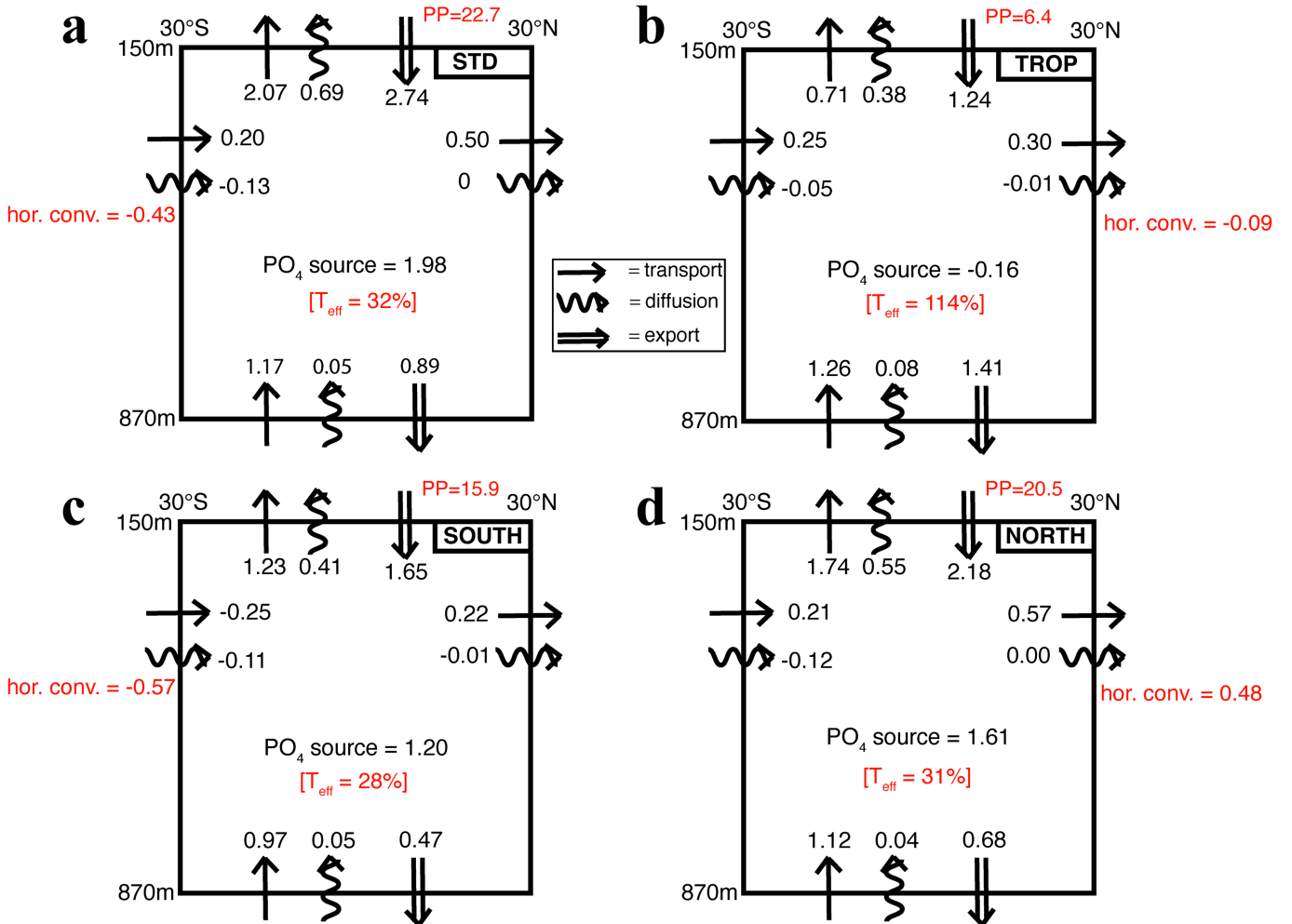
**Extended Data Fig. 3 | Distribution of  $\text{PO}_4^{3-}$  over full depth range.** Zonally-averaged  $\text{PO}_4^{3-}$  simulated by PISCES-v2<sup>27</sup> over the full ocean depth range 0–5000 m: (a) For the control simulation STD, (b) for the PERT\_TROP

simulation; (c) for the PERT\_SOUTH simulation; and (d) for the PERT\_NORTH simulation. Units are  $\mu\text{mol L}^{-1}$  for all panels.



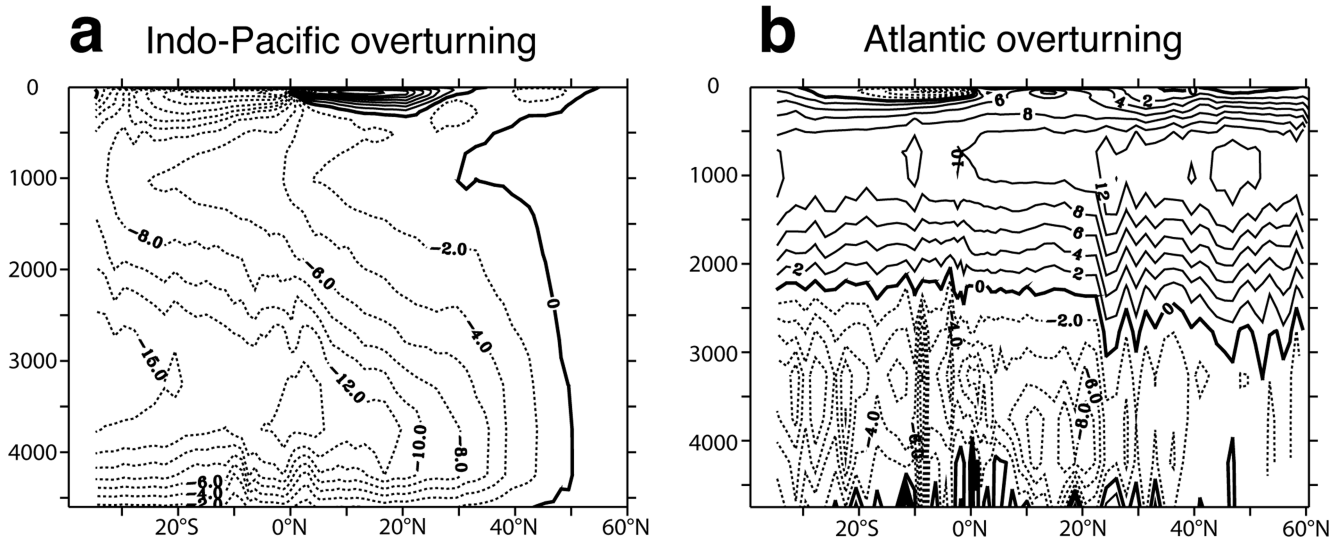
**Extended Data Fig. 4 | Distribution of  $\text{PO}_4^{3-}$  and perturbation anomalies over 0–1,800 m.** Zonally-averaged  $\text{PO}_4^{3-}$  simulated by PISCES-v2<sup>27</sup> over the ocean depth range 0–1800 m: (a) STD, (b) perturbation for PERT\_TROP

(PERT\_TROP minus STD); (c) perturbation for PERT\_SOUTH (PERT\_SOUTH minus STD); (d) perturbation for PERT\_NORTH (PERT\_NORTH minus STD). Units are  $\mu\text{mol L}^{-1}$  for all panels.



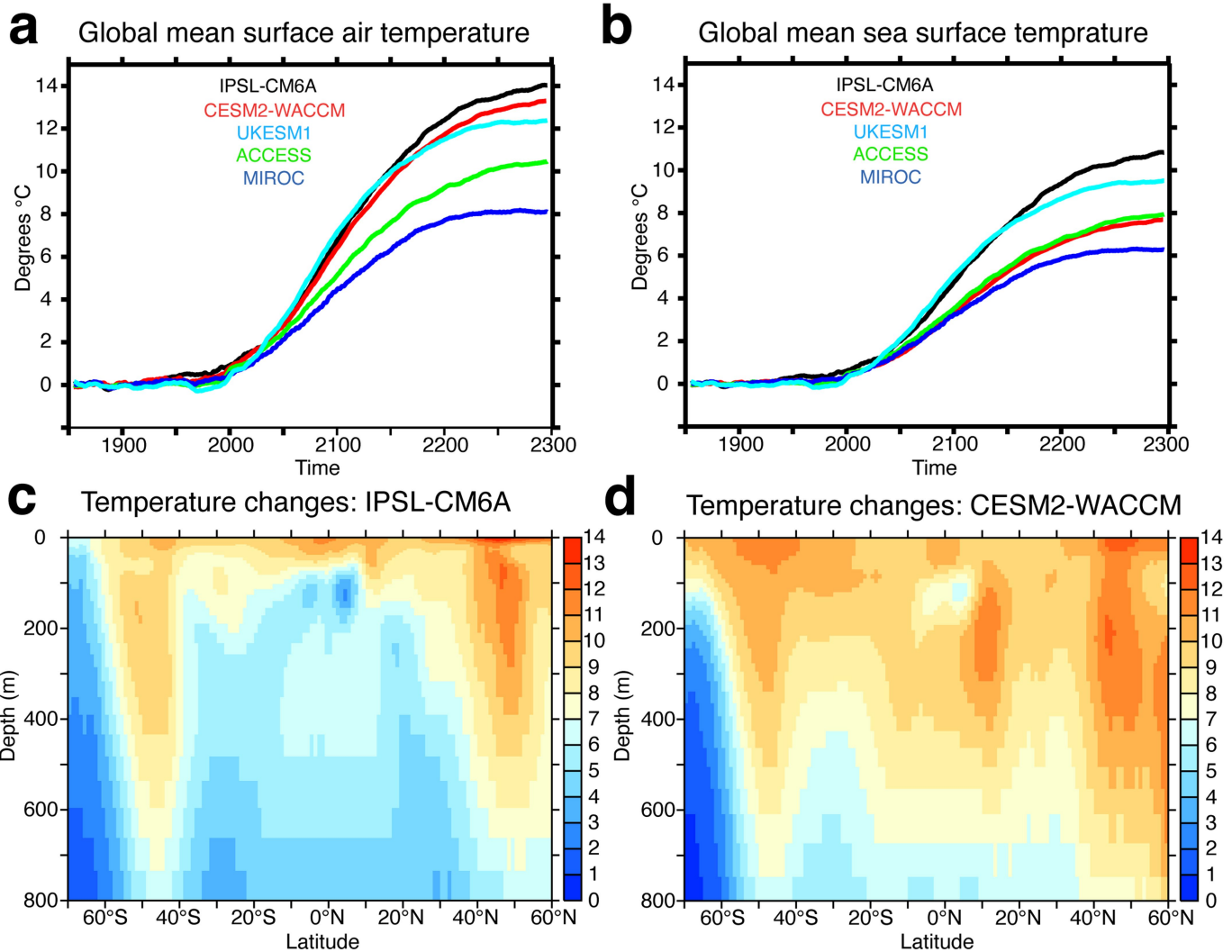
**Extended Data Fig. 5 | Coarse-grained view of modelled PO<sub>4</sub><sup>3-</sup> fluxes about the low-latitude mesopelagic domain (LLMD).** Fluxes are shown from the PISCES-v2<sup>27</sup> model simulations. The boundary fluxes and interior sources of PO<sub>4</sub><sup>3-</sup> for the domain bounded by 30°S–30°N and 150 m–870 m for (a) STD, (b) PERT\_TROP, (c) PERT\_SOUTH, and (d) PERT\_NORTH. The domain for each case is the same as that used in Fig. 3. The lateral exchanges for each case represent net fluxes, and thereby account for the effects of gyre recirculation

across 30°S and 30°N. Shown in red are the transfer efficiency, defined as the ratio of export flux across 870 m to the export flux across 150 m, and the net horizontal convergence (hor. conv.) from the LLMD domain across the meridional boundaries at 30°S and 30°N, and PP in units of PgCyr<sup>-1</sup>. Fluxes are for PO<sub>4</sub><sup>3-</sup>, but shown in carbon units of PgCyr<sup>-1</sup> to be consistent with units typically used for export and PP.



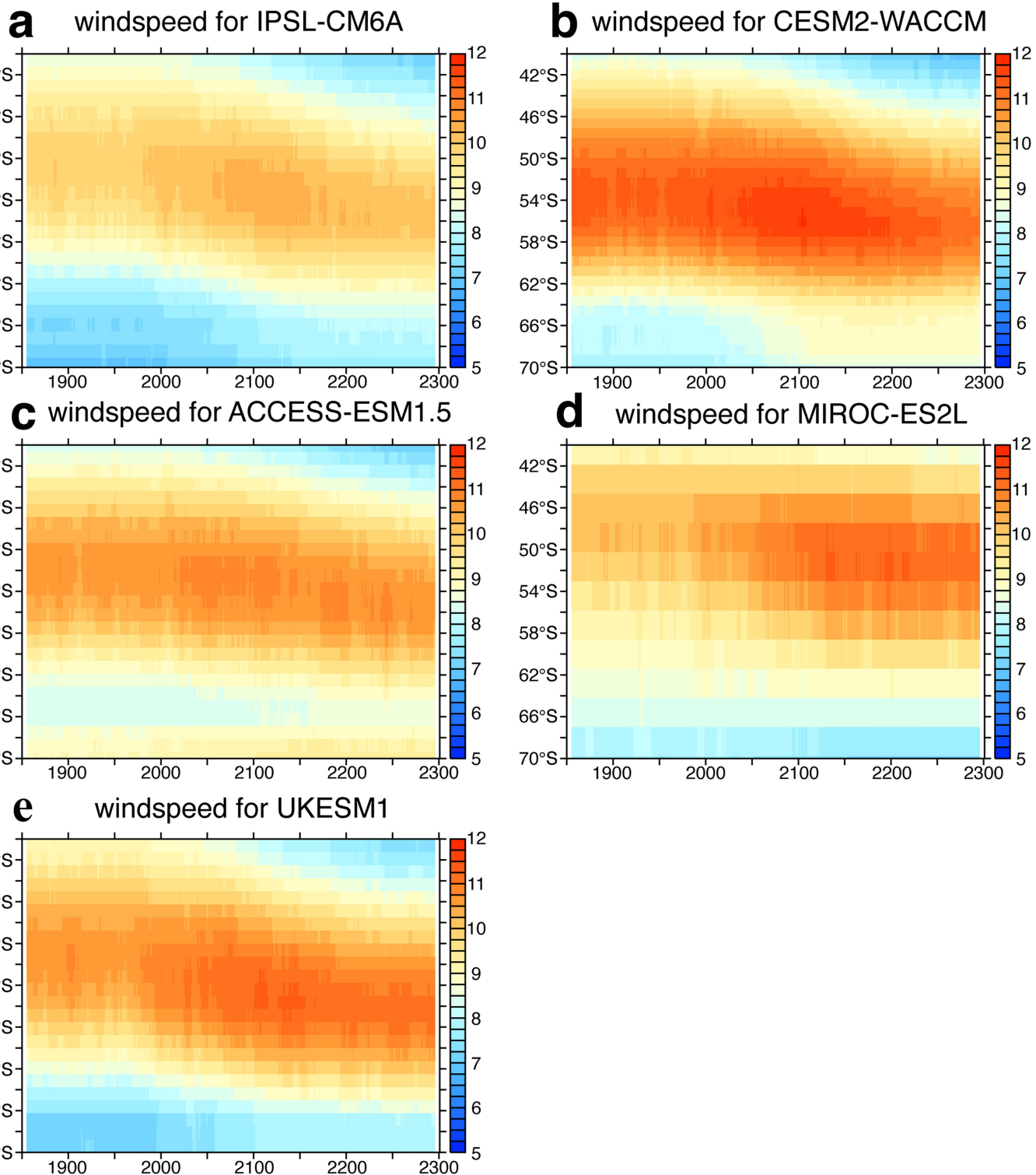
**Extended Data Fig. 6 | Large-scale ocean overturning structures that promote  $\text{PO}_4^{3-}$  upwelling.** Meridional overturning streamfunction for ORCA2 configuration of NEMO-LIM<sup>27</sup> for (a) the Indo-Pacific basin and (b) the Atlantic basin. Units are Sverdrups (Sv, or  $10^6 \text{ m}^3 \text{s}^{-1}$ ). Contour intervals for both cases are

(-30, -25, -20, -15, -12, -10, -8, -6, -4, -2, 0, 2, 4, 6, 8, 10, 12, 15, 20, 25, 30) in order to emphasize both the deep upwelling amplitude and the strength of the Indo-Pacific Subtropical Cells<sup>22</sup> within the thermocline.



**Extended Data Fig. 7 | Transients in temperature state of CMIP6 models under extended simulations to 2300.** Evolution of changes in temperature relative to the respective 1850–1899 mean for (a) globally-averaged 2 m air temperature, and (b) globally-averaged sea surface temperature for five CMIP6 models: [IPSL-CM6A<sup>16</sup>, CESM2-WACCM<sup>17</sup>, UKESM1<sup>18</sup>, ACCESS-ESM1.5<sup>19</sup>, and

MIROC-ES2L<sup>20</sup>] run to 2300 under historical/SSP5-8.5 forcing<sup>21</sup>. Changes in zonally averaged potential temperature between a 1990s climatology and a 2290 s climatology for two of the models: (c) IPSL-CM6A and (d) CESM2-WACCM. The units for all panels are °C.



**Extended Data Fig. 8 | Meridional shifts in Southern Ocean latitude of maximum wind speed for CMIP6 models.** The panels show for each ESM listed in Extended Data Table 1 the zonally-averaged monthly-mean windspeed (variable sfcwind) over 70°S-40°S of the five CMIP6 models are IPSL-CM6A<sup>16</sup>,

CESM2-WACCM<sup>17</sup>, UKESM1<sup>18</sup>, ACCESS-ESM1.5<sup>19</sup>, and MIROC-ES2L<sup>20</sup> under historical/SSP5-8.5 forcing<sup>21</sup>, and a 10-year running mean has been applied to filter seasonal and interannual variations. Units are  $\text{m s}^{-1}$ .

**Extended Data Table 1 | Deconvolution of  $\text{PO}_4^{3-}$  fluxes for the LLMD into preformed and regenerated components**

STD PERT_SOUTH PERT_TROP	Preformed- $\text{PO}_4^{3-}$ (PgC yr <sup>-1</sup> )	Regenerated- $\text{PO}_4^{3-}$ (PgC yr <sup>-1</sup> )	SO-Preformed- $\text{PO}_4^{3-}$ (PgC yr <sup>-1</sup> )	LL-regenerated- $\text{PO}_4^{3-}$ (PgC yr <sup>-1</sup> )
Vertical transport 150m	0.95 0.39 0.57	1.80 1.23 0.52	0.93 0.29 0.51	1.47 0.98 0.31
Vertical transport 870m	0.76 0.59 0.71	0.45 0.42 0.63	0.73 0.54 0.66	0.32 0.18 0.50
Lateral convergence into LLMD across 30°S and 30°N over 150m-870m	0.19 -0.17 0.06	-0.63 -0.41 -0.18	0.20 -0.23 0.03	-0.89 -0.45 -0.37

This is considered for the STD, PERT\_SOUTH, and PERT\_TROP simulations by the addition of four new tracers in PISCES-v2<sup>27</sup> following a previously published method<sup>14</sup> (see Methods for more details). Lateral convergence is positive for the case where there is a net equatorward transport for the sum of transports integrated over both 30°S and 30°N within the depth range 150m–870m. Units for all fluxes of  $\text{PO}_4^{3-}$  are in carbon units of PgC yr<sup>-1</sup> where a C:P ratio of 122:1 has been used for the conversion with PISCES-v2 output.

# Article

**Extended Data Table 2 | Thermocline nutrient retention for two Earth system models**

	EPC_150m (Pg C yr <sup>-1</sup> )	EPC_870m (Pg C yr <sup>-1</sup> )	Transfer Efficiency	Accumulation (Pg C yr <sup>-1</sup> )
<b>IPSL_CM6A</b>				
1890s	2.98	0.80	27%	2.18
1990s	2.92 (-2%)	0.77 (-4%)	26%	2.14 (-1%)
2090s	2.78 (-7%) <b>2.90 (-3%)</b>	0.68 (-16%) <b>0.74 (-8%)</b>	24% <b>25%</b>	2.10 (+3%) <b>2.16 (-1%)</b>
2190s	2.94 (-1%) <b>2.94 (-1%)</b>	0.67 (-16%) <b>0.73 (-8%)</b>	23% <b>25%</b>	2.27 (+4%) <b>2.20 (+1%)</b>
2290s	3.00 (+0.3%) <b>2.94 (-1%)</b>	0.63 (-21%) <b>0.73 (-8%)</b>	21% <b>25%</b>	2.36 (+8%) <b>2.21 (+1%)</b>
<b>CESM2-WACCM</b>				
1890s	3.14	0.82	26%	2.32
1990s	3.12 (-2%)	0.81 (-1%)	26%	2.31 (+0%)
2090s	2.90 (-8%) <b>3.05 (-3%)</b>	0.83 (+1%) <b>0.84 (+2%)</b>	29% <b>28%</b>	2.07 (-11%) <b>2.21 (-5%)</b>
2190s	2.23 (-29%) <b>2.95 (-6%)</b>	0.66 (-20%) <b>0.82 (+0%)</b>	30% <b>28%</b>	1.57 (-32%) <b>2.13 (-8%)</b>
2290s	1.96 (-38%) <b>2.95 (-6%)</b>	0.59 (-28%) <b>0.82 (+0%)</b>	30% <b>28%</b>	1.37 (-41%) <b>2.13 (-8%)</b>

Centennial-timescale changes in thermocline retention of carbon in IPSL-CM6A<sup>16</sup> and CESM2-WACCM<sup>17</sup>. Identified using changes with reference depths of 150 m and 870 m, and integrated over 30°S–30°N under historical/SSP5-8.5 forcing (black text) (see Fig. 4c) and SSP1-2.6 (red text)<sup>21</sup>. Transfer efficiency is defined as the EPC\_870m/EPC\_150m, reflecting the efficiency with which the biological pump transits the depth range 150m–870m. Accumulation rate is the difference EPC\_150m-EPC\_870m. Fluxes (EPC\_150m, EPC\_870m, and Accumulation) are for carbon in carbon units (PgC yr<sup>-1</sup>). For the fluxes, percentages shown in parentheses represent temporal changes relative to the 1890s.